Electronic Materials Letters (2025) 21:87–93
https://doi.org/10.1007/s13391-024-00524-w

ORIGINAL ARTICLE – NANOMATERIALS

Synthesis of Core/Shell WO_3/WS_2 Heterostructure Nanowires with Negative Photo-Responsiveness

Yu-Jin Song[1] · Changhyeon Yoo[2] · Camellia Schwartzman[3] · Han-Kyun Shin[1] · Hyoung J. Cho[4] · Yeonwoong Jung[2,5,6] · Jung Han Kim[1]

Received: 23 July 2024 / Accepted: 19 September 2024 / Published online: 10 October 2024

Abstract

WO_3/WS_2 core/shell nanowires were synthesized using a scalable fabrication method by combining wet chemical etching and chemical vapor deposition (CVD). Initially, WO_3 nanowires were formed through wet chemical etching using a potassium hydroxide (KOH) solution, followed by oxidation at 650 °C. These WO_3 nanowires were then sulfurized at 900 °C to form a WS_2 shell, resulting in WO_3/WS_2 core/shell nanowires with diameters ranging from 90 to 370 nm. The synthesized nanowires were characterized using scanning electron microscopy (SEM), Raman, energy-dispersive X-ray spectroscopy (EDS), X-ray diffractometry (XRD), and transmission electron microscopy (TEM). The shell is composed of 2D WS_2 layers with uniformly spaced 2D layers as well as the atomically sharp core/shell interface of WO_3/WS_2. Notably, the WO_3/WS_2 heterostructure nanowires exhibited a unique negative photoresponse under visible light (405 nm) illumination. This negative photoresponse highlights the importance of interface engineering in these heterostructures and demonstrates the potential of WO_3/WS_2 core/shell nanowires for applications in photodetectors and other optoelectronic devices.

Graphical Abstract

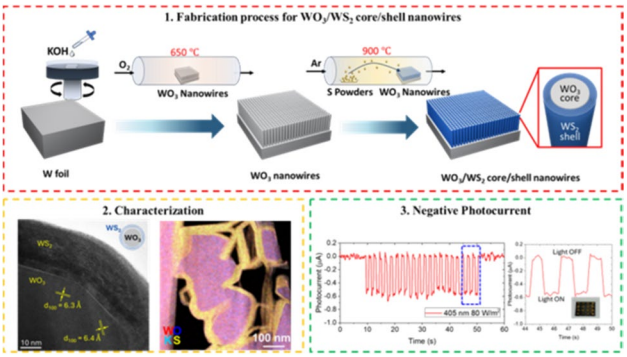

Yu-Jin Song and Changhyeon Yoo have contributed equally to this work.

✉ Changhyeon Yoo
chang-hyeon.yoo@ucf.edu

✉ Yeonwoong Jung
yeonwoong.jung@ucf.edu

✉ Jung Han Kim
junghankim@dau.ac.kr

[1] Department of Materials Science and Engineering, Dong-A University, Saha-Gu, Busan 49315, Republic of Korea

[2] NanoScience Technology Center, University of Central Florida, Orlando, FL 32826, USA

[3] Department of Physics and Astronomy, Macalester College, Saint Paul, MN 55105, USA

[4] Department of Mechanical and Aerospace Engineering, University of Central Florida, Orlando, FL 32816, USA

[5] Department of Materials Science and Engineering, University of Central Florida, Orlando, FL 32816, USA

[6] Department of Electrical and Computer Engineering, University of Central Florida, Orlando, FL 32816, USA

Keywords WO_3/WS_2 nanowires · Heterostructure nanowires · Core/shell nanowires · Negative photoresponse

1 Introduction

Nanowires have shown great potential for various applications, including supercapacitors [1, 2], transparent films [3, 4], electronics [5], gas sensors [6–8], antibacterial applications [9, 10], and in photocathodes [11] or electrocatalysts for hydrogen production [12]. Their physical structure, with high length-to-diameter ratios, is ideal for sensors, lasers, and LEDs due to the large surface area-to-volume ratio [13, 14]. The synthesis method significantly influences the physical and chemical properties of nanowires.

Transition Metal Dichalcogenides (TMDs), with the chemical formula MX_2 (where M represents a transition metal and X represents a chalcogen), exhibit unique properties [15, 16]. When at the monolayer level, the bandgap of TMDs transitions from indirect to direct [17], significantly enhancing their light-matter interaction and resulting in unique excitonic effects. This transition is particularly notable in WS_2, where the bandgap changes from 1.32 eV in the bulk form to 2.03 eV at the monolayer level, which substantially improves photoluminescence intensity and optical properties [18, 19]. With its tunable bandgap and high wear resistance, WS_2 is considered suitable for applications in supercapacitors, solar cells, electro/photocatalysts, and various types of batteries [20].

In our study, we used wet chemical etching to remove parts of the bulk material, resulting in WO_3/WS_2 core/shell nanowires. This top-down approach facilitates the scalable fabrication of ordered nanowire arrays. Starting with W foil, we synthesized core/shell nanowires to produce integrated one-body structures and sulfurized the surface using the chemical vapor deposition (CVD) method to form WS_2 shells. The fabricated WO_3/WS_2 core/shell nanowires were tested for a photoresponse. These nanowires demonstrated a negative photoresponse, where conductivity decreases upon illumination. This finding emphasizes the importance of interface engineering and the unique properties of 2D materials.

2 Experimental Methods

The growth of the WO_3/WS_2 core/shell nanowires was carried out in the order shown in Fig. 1. Initially, a 100 µm thick W foil (Nilaco, Japan) was drop-casted with a 10 wt% potassium hydroxide (KOH) solution (≥ 85%, Duksan, South Korea) using a spin-coater. The drop-casted foil was then oxidized at 650 °C for 40 min, forming WO_3 nanowires. Subsequently, sulfurization was performed using the CVD method at 900 °C for 40 min with an Ar gas flow of 100 sccm, synthesizing the WO_3/WS_2 core/shell nanowires.

The morphologies and microstructures of WO_3/WS_2 core/shell nanowires are analyzed by field emission scanning electron microscopy (FE-SEM) (Scios2, Thermo Fisher Scientific). Raman spectroscopy characterization was performed using a Horiba LabRAM HR Evolution Nano system equipped with a 532 nm laser source. X-ray diffractometer (XRD) (EMPYREAN, Malvern Panalytical) was conducted using a 2 T-omega scan (10–90°2Th., step size 0.0260°2Th.) and Cu K-α (0.154060 nm) radiation. For the preparation of the cross-sectional transmission electron microscope (TEM) sample, we employed a Dual-Beam focused ion beam (FIB) (Scios2, Thermo Fisher Scientific) using a 30 kV gallium (Ga) ion beam for the lift-out technique. The sample was then examined using a high-resolution (HR) TEM (Talos F200X, Thermo Fisher Scientific) equipped with energy-dispersive X-ray spectroscopy (EDS), operating at an acceleration voltage of 200 kV. Photoresponsiveness measurements were performed using a 405 nm laser source with a power intensity of 80 W/m^2, while prepared nanowires were connected to a custom-built probe station and a semiconductor

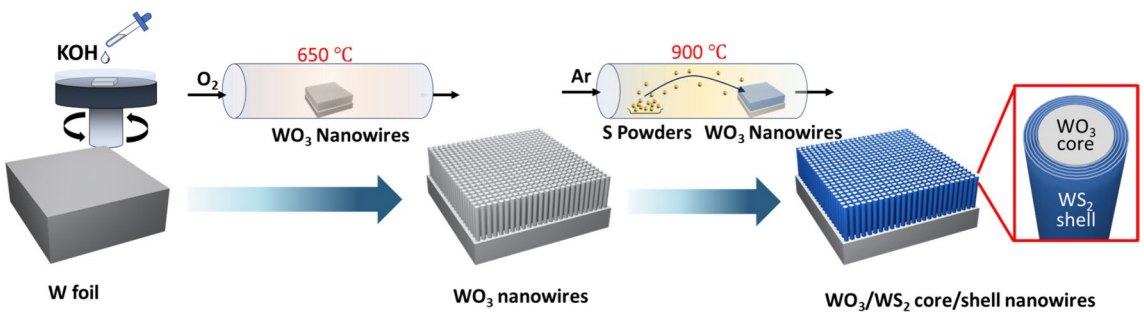

Fig. 1 Schematic of the fabrication process for WO_3/WS_2 nanowires, including KOH etching, oxidation, and CVD sulfurization, leading to WO_3 nanowires and the WS2 shell formation

parameter analyzer (HP 4156A) for two-terminal electrical measurements.

3 Results and Discussion

Figure 2 presents the characterization of WO_3 nanowires and WO_3/WS_2 core/shell nanowires. Figure 2a demonstrates that core/shell nanowires were uniformly synthesized across the entire surface, centered around the core. After oxidation, the areas coated with KOH solution turned white, while after sulfurization, they exhibited a blue color on the surface. Figure 2b shows SEM images of densely packed WO_3 nanowires, which offer a large surface area, with diameters of approximately 200 nm and lengths of 8–10 µm, formed after KOH etching of the W substrate and oxidation at 650 °C. Figure 2c exhibits the top-view SEM image of the WO_3 nanowires after sulfurization at 900 °C. The morphology of the WO_3/WS_2 nanowires resembled disordered "forest-like" clumps, with many nanowires oriented in different directions and exhibiting varying diameters.

The structural quality of WO_3/WS_2 nanowires was further assessed using Raman spectroscopy with a 532 nm laser at room temperature. Figure 2d presents the Raman spectra obtained from WO_3/WS_2 nanowires on a W foil. The Raman bands located at 420 cm^{-1} and 350 cm^{-1} correspond to the W−S stretching vibrations of WS_2, associated with the A_{1g} and E^1_{2g} modes, respectively. Additionally, the Raman spectra exhibit peaks at 321 and 581 cm^{-1}, indicative of the first-order and second-order Raman modes of 2D WS_2. A minor peak at 700 cm^{-1} is attributed to the stretching modes of O–W–O bonds [21], confirming the presence of WO_3 alongside WS_2. Notably, prior to sulfurization, Raman characterization of the as-prepared WO_3 nanowires distinctly reveals the stretching modes of O–W–O bonds [22]. The Raman spectra at various points are shown in Supplementary Information Fig. S1.

XRD analysis was subsequently conducted to examine the structures of the WO_3 and WO_3/WS_2 samples. Figure 2e indicates that the peaks of WO_3 correspond to hexagonal WO_3 (ICDD 01-085-2460). The XRD patterns are dominated by sharp (002) diffraction peaks, signifying a high degree of crystallinity and strong orientation along the c-axis of the crystal structure. In Fig. 2f, the XRD patterns reveal peaks at 14.3°, 28.0°, and 33.8°, characteristic of WS_2 (ICDD 01-084-1399), corresponding to the (003), (006), and (012) crystal planes, respectively. The peaks indicate that the WO_3/WS_2 nanowires were successfully synthesized. Both samples show prominent WO_3 peaks at 23.6° and 48.2°, which are associated with the (002) and (004) planes. The peak corresponding to WS_2 is relatively weaker than WO_3, owing to the thinness of the WS_2 layer. Additionally, the (200) lattice plane of the W substrate is consistently observed at 58.3°.

The microstructures of WO_3/WS_2 core/shell nanowires were examined cross-sectionally using TEM Fig. 3a presents a low-magnification cross-sectional bright field (BF). The TEM image of the nanowires revealed a cuboid-like morphology with a WO_3 core of approximately 300 nm in diameter and a WS_2 shell of around 30 nm thick. The detailed crystallinity of the nanowires was investigated by high-resolution (HR-) TEM. Figure 3b shows the cross-sectional HR-TEM image of the nanowires along with the fast Fourier transform (FFT) of each segment. The HR-TEM image shows that the shell is composed of 2D WS_2 layers with uniformly spaced 2D layers as well as

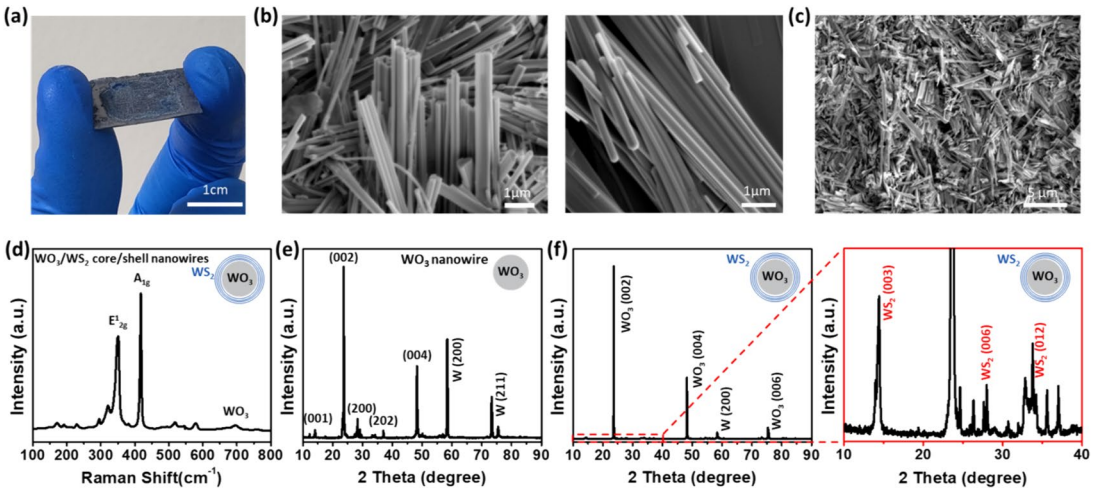

Fig. 2 Characterization of WO_3 nanowires and WO_3/WS_2 core/shell nanowires. **a** Optical image of the large-area sample. SEM images of **b** WO_3 nanowires before sulfurization and **c** WO_3/WS_2 nanowires after the CVD sulfurization. **d** Raman spectra showing peaks of both WS_2 and WO_3. XRD patterns of **e** WO_3 nanowires and **f** WO_3/WS_2 nanowires, confirming the heterostructure

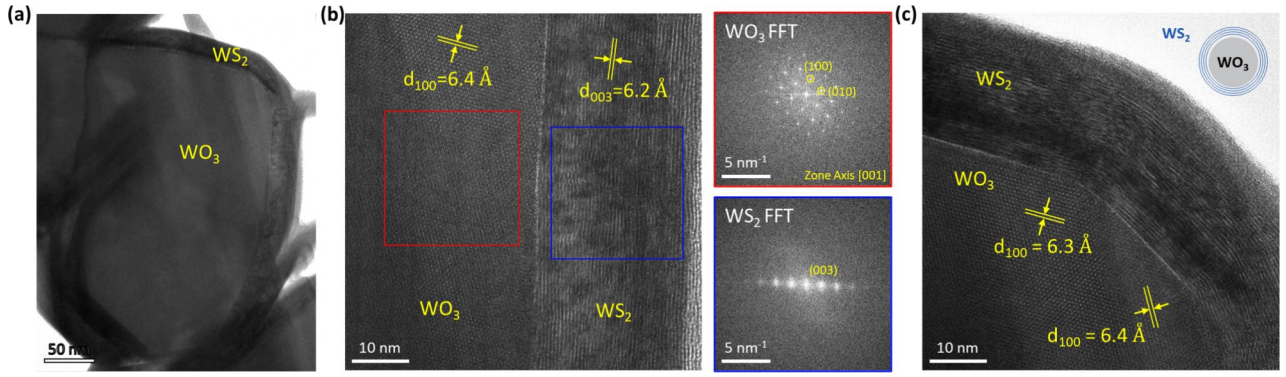

Fig. 3 Cross-sectional TEM characterization of the WO_3/WS_2 nanowires. **a** Low-magnification TEM image of WO_3/WS_2 core/shell nanowire. **b** HR-TEM image of WO_3/WS_2 nanowires, with FFT analysis of each material (red for WO_3 and blue for WS_2). **c** HR-TEM image showing the WS_2 layer-by-layer structure

the atomically sharp core/shell interface of WO_3/WS_2. The 6.4 Å spacing corresponds to the (100) crystal plane of hexagonal WO_3, while the stacking of WS_2 (003) layers exhibits an interplanar spacing of 6.2 Å. The red FFT reveals the presence of the highly crystalline hexagonal structure of WO_3, which is investigated along the [001] zone axis, while the blue FFT shows the layer-by-layer formation of WS_2. Figure 3c illustrates the WS_2 shell structure, consistently approximately 30 nm thick and composed of roughly 30 layers, formed around the WO_3 nanowire in a layer-by-layer arrangement, encapsulating the WO3 core.

To further examine the elemental distribution within the WO_3/WS_2 core/shell structure, EDS-STEM was employed on the WO_3/WS_2 nanowires. Figure 4a shows that high-angle annular dark field (HAADF) images confirmed the successful synthesis of a WO_3/WS_2 heterostructure, with 2D WS_2 layers forming a shell on the outer surface of the WO_3 core, formed through etching and oxidation of the W foil substrate. The EDS elemental mapping in Fig. 4b, taken at relatively low magnification, clearly shows the localized distribution of W, O, and S. W and O are concentrated in the core, while S is predominantly in the shell, further verifying the core/shell structure. Figure 4c presents qualitative

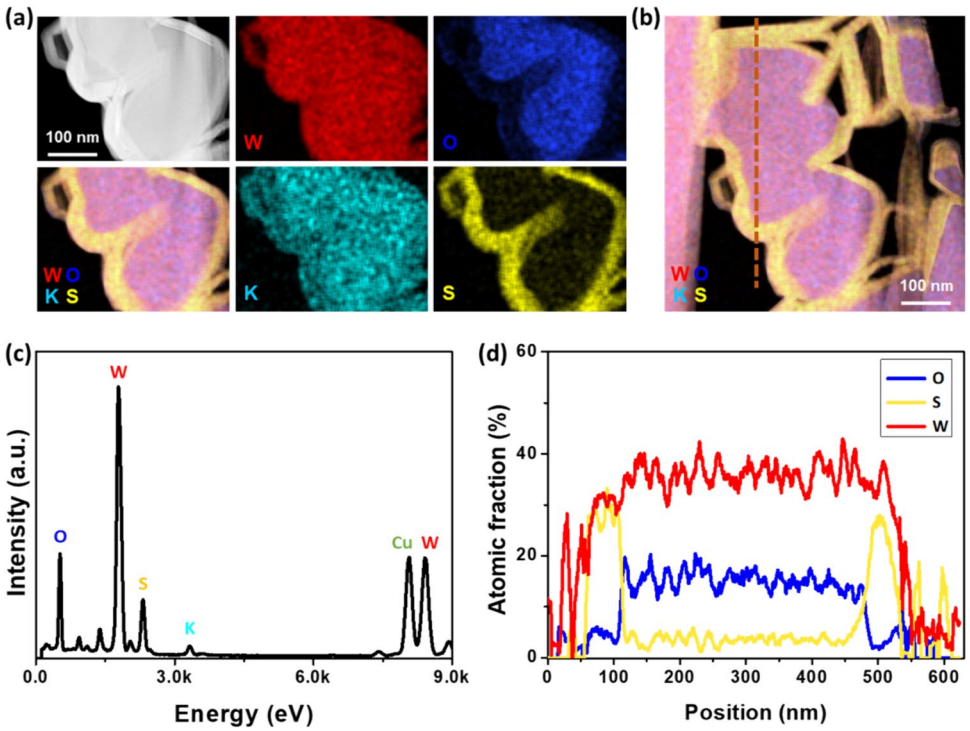

Fig. 4 EDS mapping images of WO_3/WS_2 nanowires of **a** each element, combined, and **b** the localized distribution of W, O, and S, showing the spatial segregation of elements within the core and shell regions. **c** EDS spectrum obtained from the nanowires, confirming the elemental composition. **d** EDS composition line profiles of O, S, and W across the WO_3/WS_2 nanowires along the line shown in **b**, further demonstrating the core/shell structure with a well-defined interface

and quantitative EDS spectrum obtained from the WO_3/WS_2 nanowires, indicating the stoichiometric distribution of elements in their areas. For a more detailed analysis, Fig. 4d displays the EDS atomic fraction of each element profiled along the line shown in Fig. 4b. This analysis confirms that an approximately 50 nm thick WS_2 shell is uniformly formed on the 400 nm diameter WO_3 core surface, demonstrating a clear and sharp interface between them. EDS point analysis showed a well-synthesized composition with W:O = 1:3 and W:S = 1:2 (Supplementary Information, Fig. S2).

Research on the negative photoresponse in WS_2 materials has gained significant attention for its potential in optoelectronic devices [23, 24]. Negative photocurrent response is the phenomenon where a material's conductivity decreases upon illumination, contrary to the typical increase observed in most materials. This has been demonstrated in layered WS_2/reduced graphene oxide hybrids under Infrared (IR) illumination [23] and in WS_2 nanosheets decorated with Au nanoparticles under 450 nm laser illumination [24].

Figure 5 illustrates the negative photodetection characteristics of WO_3/WS_2 under 405 nm visible light, using a continuous wave (CW) laser source at an intensity of 80 W/m^2 with 1 s on/off cycles. In Fig. 5a, the overall photodetection response is depicted, highlighting the material's ability to detect light and showing negative photoresponse for a 405 nm laser source and applied bias of 1 mV. A magnified view of three representative light cycles is shown in Fig. 5b, providing a closer look at the material's responsiveness to periodic light exposure. The inset image reveals the actual sample with Au contacts, demonstrating the physical setup used for the measurements. Figure 5c illustrates the photocurrent versus time at varied bias voltages of 0.1, 1, 2, and 5 mV, where no significant photoresponse was observed at 10 mV, showcasing the material's performance under different electrical conditions. Finally, Fig. 5d details the dependence of the photocurrent on the applied bias voltage, emphasizing the relationship between the electrical bias and the photocurrent.

Negative photoresponse in WS_2 can be attributed to several mechanisms, primarily involving charge transfer processes and the interaction between different materials or nanostructures. It is proposed that upon illumination, photogenerated carriers are trapped at interface or defect states, reducing overall conductivity [25, 26]. This trapping, likely influenced by the band alignment and interface states between the WO_3 1D core and WS_2 2D shell,

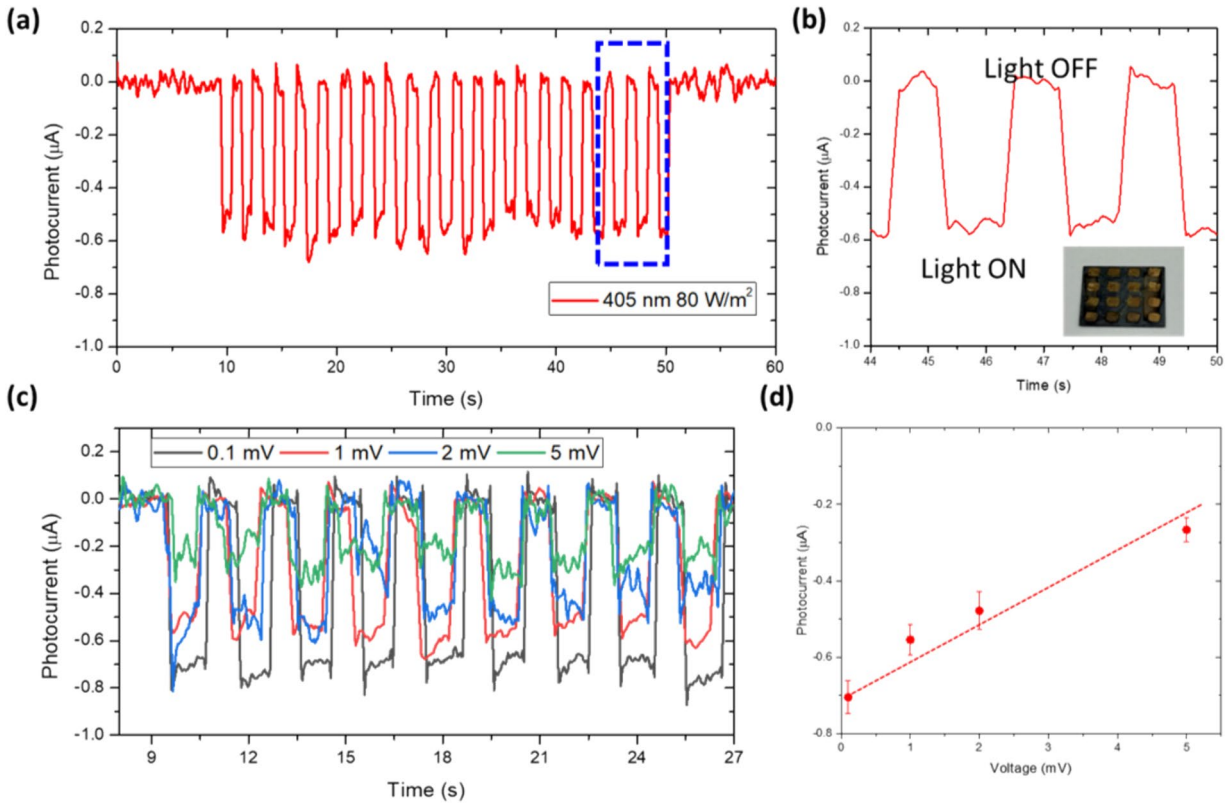

Fig. 5 **a** Negative photoresponse of WO_3/WS_2 under 405 nm visible light at a laser intensity of 80 W/m^2 with 1 s on/off cycles under a 1 mV bias. **b** Magnified view of three representative light cycles, providing a closer look at the material's negative photoresponse behavior. Inset: Actual sample with Au contacts. **c** Photocurrent versus time at varied bias voltages (1 s on/off cycles). **d** Dependence of generated photocurrent on the applied bias voltage, illustrating the relationship between electrical bias and photoresponse

prevents carriers from contributing to current flow, leading to a negative photoresponse upon 405 nm illumination. The observed negative photoresponse in the WO_3/WS_2 core/shell heterostructure, potentially enhanced by charge trapping at the interface between WO_3 and WS_2, is assumed to be driven by the staggered band structure between two materials [23, 24, 27]. This alignment facilitates charge separation and may lead to electron trapping at the interface, thereby reducing the overall carrier density under illumination. This behavior seems consistent with previously reported results in WS_2/Au nanoparticle-decorated nanosheets and WS_2/RGO hybrids, where interface states play a role in trapping photogenerated carriers and suppressing photocurrent under light exposure [23, 24].

4 Conclusion

In summary, WO_3/WS_2 core/shell nanowires were synthesized by CVD sulfurization at 900 °C following KOH solution wet chemical etching and oxidation. The morphological characteristics and elemental distribution of the WO_3/WS_2 core/shell heterostructures were examined using SEM, Raman, XRD, TEM, and EDS. The WO_3/WS_2 heterostructure nanowires exhibit a distinct negative photoresponse under visible light illumination. This behavior, combined with the detailed morphological and structural analysis, indicates the potential of these nanowires for applications in photodetectors and other optoelectronic devices. The successful synthesis of these heterostructures demonstrates a robust method for creating advanced nanomaterials with tunable properties, paving the way for further exploration and development in photodetection and optoelectronics.

Supplementary Information The online version contains supplementary material available at https://doi.org/10.1007/s13391-024-00524-w.

Acknowledgements H.J.C. acknowledges financial support from the National Science Foundation under Grant OISE: 2153228. J.H.K. acknowledges support from the Korea Institute of Energy Technology Evaluation and Planning (KETEP) and the Ministry of Trade, Industry & Energy (MOTIE) of the Republic of Korea (NO. 20224000000400).

Author Contributions Yu-Jin Song: Writing of original draft, Sample Preparation, Characterization, Visualization, Formal analysis, Data curation. Changhyeon Yoo: Writing of original draft, review, and editing, Characterization, Visualization, Formal analysis, Data curation. Camellia Schwartzman: Sample preparation. Characterization. Han-Kyun Shin: Sample preparation, Characterization. Hyoung Jin Cho: Writing of review & editing, Supervision. Yeonwoong Jung: Writing of review & editing, Supervision, Characterization, Visualization, Conceptualization. Jung Han Kim: Writing of review & editing, Characterization, Supervision.

Data Availability Data will be made available on request.

Declarations

Conflict of interest The authors declare that they have no known competing financial interests or personal relationships that could have appeared to influence the work reported in this paper.

References

1. Choudhary, N., Li, C., Chung, H.-S., Moore, J., Thomas, J., Jung, Y.: High-performance one-body core/shell nanowire supercapacitor enabled by conformal growth of capacitive 2D WS_2 Layers. ACS Nano **10**, 10726–10735 (2016). https://doi.org/10.1021/acsnano.6b06111
2. Xiao, X., Ding, T., Yuan, L., Shen, Y., Zhong, Q., Zhang, X., Cao, Y., Hu, B., Zhai, T., Gong, L., Chen, J., Tong, Y., Zhou, J., Wang, Z.L.: WO_{3-x}/MoO_{3-x} core/shell nanowires on carbon fabric as an anode for all-solid-state asymmetric supercapacitors. Adv. Energy Mater. **2**, 1328–1332 (2012). https://doi.org/10.1002/aenm.201200380
3. Zhong, J., Wang, Y.: Transparent conductive silver nanowires films on glass substrate. Micro Nano Lett. **15**, 988–991 (2020). https://doi.org/10.1049/mnl.2019.0685
4. Qiu, J., Wang, X., Ma, Y., Yu, Z., Li, T.: Stretchable transparent conductive films based on Ag nanowires for flexible circuits and tension sensors. ACS Appl. Nano Mater. **4**, 3760–3766 (2021). https://doi.org/10.1021/acsanm.1c00217
5. Kim, J.H., Kim, J.G., Song, J., Bae, T.-S., Kim, K.-H., Lee, Y.-S., Pang, Y., Oh, K.H., Chung, H.-S.: Investigation of the growth and in situ heating transmission electron microscopy analysis of Ag_2S-catalyzed ZnS nanowires. Appl. Surf. Sci. **436**, 556–561 (2018). https://doi.org/10.1016/j.apsusc.2017.12.045
6. Meng, D., Shaalan, N.M., Yamazaki, T., Kikuta, T.: Preparation of tungsten oxide nanowires and their application to NO_2 sensing. Sens. Actuators B Chem. **169**, 113–120 (2012). https://doi.org/10.1016/j.snb.2012.04.001
7. Chen, P.-R., Fu, H.-W., Yang, S.-M., Lu, K.-C.: Chemical vapor deposition-fabricated manganese-doped and potassium-doped hexagonal tungsten trioxide nanowires with enhanced gas sensing and photocatalytic properties. Nanomaterials **12**, 1208 (2022). https://doi.org/10.3390/nano12071208
8. Park, S., An, S., Ko, H., Lee, S., Lee, C.: Synthesis, structure, and UV-enhanced gas sensing properties of Au-functionalized ZnS nanowires. Sens. Actuators B Chem. **188**, 1270–1276 (2013). https://doi.org/10.1016/j.snb.2013.07.076
9. Kim, T.I., Kim, J., Park, I.J., Cho, K.O., Choi, S.Y.: Chemically exfoliated 1T-phase transition metal dichalcogenide nanosheets for transparent antibacterial applications. 2D Mater. **6**, 025025–025028 (2019). https://doi.org/10.1088/2053-1583/ab070e
10. Ghasempour, F., Azimirad, R., Amini, A., Akhavan, O.: Visible light photoinactivation of bacteria by tungsten oxide nanostructures formed on a tungsten foil. Appl. Surf. Sci. **338**, 55–60 (2015). https://doi.org/10.1016/j.apsusc.2015.01.217
11. Huang, Z., Wang, C., Chen, Z., Meng, H., Lv, C., Chen, Z., Han, R., Zhang, C.: Tungsten sulfide enhancing solar-driven hydrogen production from silicon nanowires. ACS Appl. Mater. Interfaces **6**, 10408–10414 (2014). https://doi.org/10.1021/am501940x
12. Lin, J.-F., Pitkänen, O., Mäklin, J., Puskas, R., Kukovecz, A., Dombovari, A., Toth, G., Kordas, K.: Synthesis of tungsten carbide and tungsten disulfide on vertically aligned multi-walled carbon nanotube forests and their application as non-Pt electrocatalysts for the hydrogen evolution reaction. J. Mater. Chem. A **3**, 14609–14616 (2015). https://doi.org/10.1039/C5TA02908B
13. Zhang, A., Zheng, G., Lieber, C.: Nanowires—building blocks for nanoscience and nanotechnology. Springer, Cham (2016)

14. Qian, F., Gradečak, S., Li, Y., Wen, C.-Y., Lieber, C.M.: Core/multishell nanowire heterostructures as multicolor, high-efficiency light-emitting diodes. Nano Lett. **5**, 2287–2291 (2005). https://doi.org/10.1021/nl051689e
15. Ko, T.-J., Wang, M., Yoo, C., Okogbue, E., Islam, M.A., Li, H., Shawkat, M.S., Han, S.S., Oh, K.H., Jung, Y.: Large-area 2D TMD layers for mechanically reconfigurable electronic devices. J. Phys. D Appl. Phys. **53**, 313002 (2020). https://doi.org/10.1088/1361-6463/ab87bb
16. Manzeli, S., Ovchinnikov, D., Pasquier, D., Yazyev, O.V., Kis, A.: 2D transition metal dichalcogenides. Nat. Rev. Mater. **2**, 17033 (2017). https://doi.org/10.1038/natrevmats.2017.33
17. Choudhary, N., Islam, M.A., Kim, J.H., Ko, T.-J., Schropp, A., Hurtado, L., Weitzman, D., Zhai, L., Jung, Y.: Two-dimensional transition metal dichalcogenide hybrid materials for energy applications. Nano Today **19**, 16–40 (2018). https://doi.org/10.1016/j.nantod.2018.02.007
18. Ernandes, C., Khalil, L., Almabrouk, H., Pierucci, D., Zheng, B., Avila, J., Dudin, P., Chaste, J., Oehler, F., Pala, M., Bisti, F., Brulé, T., Lhuillier, E., Pan, A., Ouerghi, A.: Indirect to direct band gap crossover in two-dimensional $WS_{2(1-x)}Se_{2x}$ alloys. njp 2D Mater. Appl. (2021). https://doi.org/10.1038/s41699-020-00187-9
19. Gusakova, J., Wang, X., Shiau, L.L., Krivosheeva, A., Shaposhnikov, V., Borisenko, V., Gusakov, V., Tay, B.K.: Electronic properties of bulk and monolayer TMDs: theoretical study within DFT framework (GVJ-2e method). Phys. Status Solidi A **214**, 1700218 (2017). https://doi.org/10.1002/pssa.201700218
20. Lei, W., Xiao, J.-L., Liu, H.-P., Jia, Q.-L., Zhang, H.-J.: Tungsten disulfide: synthesis and applications in electrochemical energy storage and conversion. Tungsten **2**, 217–239 (2020). https://doi.org/10.1007/s42864-020-00054-6
21. Cheng, Z., Wang, Z., Shifa, T.A., Wang, F., Zhan, X., Xu, K., Liu, Q., He, J.: Au plasmonics in a WS_2-Au-$CuInS_2$ photocatalyst for significantly enhanced hydrogen generation. Appl. Phys. Lett. (2015). https://doi.org/10.1063/1.4937008
22. Balaji, S., Djaoued, Y., Albert, A.-S., Ferguson, R.Z., Brüning, R.: Hexagonal tungsten oxide based electrochromic devices: spectroscopic evidence for the Li ion occupancy of four-coordinated square windows. Chem. Mater. **21**, 1381–1389 (2009). https://doi.org/10.1021/cm8034455
23. Ratha, S., Simbeck, A.J., Late, D.J., Nayak, S.K., Rout, C.S.: Negative infrared photocurrent response in layered WS_2/reduced graphene oxide hybrids. Appl. Phys. Lett. (2014). https://doi.org/10.1063/1.4903780
24. Kim, B.H., Kwon, S.H., Gu, H.H., Yoon, Y.J.: Negative photoconductivity of WS_2 nanosheets decorated with Au nanoparticles via electron-beam irradiation. Phys. E Low-Dimens. Syst. Nanostruct. **106**, 45–49 (2019). https://doi.org/10.1016/j.physe.2018.10.008
25. Yiyun, Z., Zhang, Y., Pan, D., Xiaoyan, Y., Jianhua, Z., Jinmin, L.: Negative photoconductive effects in uncooled InAs nanowire photodetectors. Front. Phys. (2021). https://doi.org/10.3389/fphy.2021.725680
26. Li, H., Alradhi, H., Jin, Z., Anyebe, E.A., Sanchez, A.M., Linhart, W.M., Kudrawiec, R., Fang, H., Wang, Z., Hu, W., Zhuang, Q.: Novel type-II InAs/AlSb core–shell nanowires and their enhanced negative photocurrent for efficient photodetection. Adv. Funct. Mater. **28**, 1705382 (2018). https://doi.org/10.1002/adfm.201705382
27. Yadav, P.V.K., Reddy, Y.A.K.: WS_2/WO_3 heterostructure-based photodetectors on SiO_2/Si for future optoelectronics. ACS Appl. Electron. Mater. **5**, 2538–2547 (2023). https://doi.org/10.1021/acsaelm.3c00013